PAPER

Rectified photocurrent in a planar ITO/graphene/ITO photodetector on SiC by local irradiation of ultraviolet light

To cite this article: Junwei Yang *et al* 2017 *J. Phys. D: Appl. Phys.* **50** 405102

View the article online for updates and enhancements.

Rectified photocurrent in a planar ITO/graphene/ITO photodetector on SiC by local irradiation of ultraviolet light

Junwei Yang[1,2]**, Liwei Guo**[1,7]**, Jiao Huang**[1]**, Qi Mao**[3]**, Yunlong Guo**[1,2]**,
Yuping Jia**[4]**, Tonghua Peng**[5]** and Xiaolong Chen**[1,2,6,7]

[1] Research & Development Center for Functional Crystals, Beijing National Laboratory for Condensed Matter Physics, Institute of Physics, Chinese Academy of Sciences, Beijing 100190, People's Republic of China
[2] University of Chinese Academy of Sciences, Beijing 100049, People's Republic of China
[3] Solid State Quantum Information and Computation Laboratory, Beijing National Laboratory for Condensed Matter Physics, Institute of Physics, Chinese Academy of Sciences, Beijing 100190, People's Republic of China
[4] State Key Laboratory of Luminescence and Applications, Changchun Institute of Optics, Fine Mechanics and Physics, Chinese Academy of Sciences, Changchun 130033, People's Republic of China
[5] TankeBlue Semiconductor Co. Ltd, Beijing, People's Republic of China
[6] Collaborative Innovation Center of Quantum Matter, Beijing, People's Republic of China

E-mail: lwguo@iphy.ac.cn and xlchen@iphy.ac.cn

CrossMark

Abstract

A rectified photocurrent behaviour is demonstrated in a simple planar structure of ITO-graphene-ITO formed on a SiC substrate when an ultraviolet (UV) light is locally incident on one of the edges between the graphene and ITO electrode. The photocurrent has similar characteristics as those of a vertical structure graphene/semiconductor junction photodiode, but is clearly different from those found in a planar structure metal–graphene–metal device. Furthermore, the device behaves multi-functionally as a photodiode with sensitive UV photodetection capability (responsivity of 11.7 mA W^{-1} at 0.3 V) and a self-powered UV photodetector (responsivity of 4.4 mA W^{-1} at zero bias). Both features are operative in a wide dynamic range and with a fast speed of response in about gigahertz. The linear I–V behaviour with laser power at forward bias and cutoff at reverse bias leads to a conceptual photodiode, which is compatible with modern semiconductor planar device architecture. This paves a potential way to realize ultrafast graphene planar photodiodes for monolithic integration of graphene-based devices on the same SiC substrate.

Keywords: graphene, ITO, SiC, planar photodetector, photodiode-like behaviour

Ⓢ Supplementary material for this article is available online

(Some figures may appear in colour only in the online journal)

1. Introduction

Since its discovery, graphene has attracted much attention in photodetectors due to its outstanding properties, such as ultrahigh carrier mobility, excellent transmittance and a wide absorption window spanning ultraviolet to infrared wavelengths [1–3]. Until today, almost all the device structures of graphene photodetectors are classified as two kinds: (1) the vertical structure, graphene/semiconductor junction [4–12], and (2) the planar structure, metal–graphene–metal configuration [13–20]. The vertical structure has many excellent advantages over the planar structure, such as high responsivity

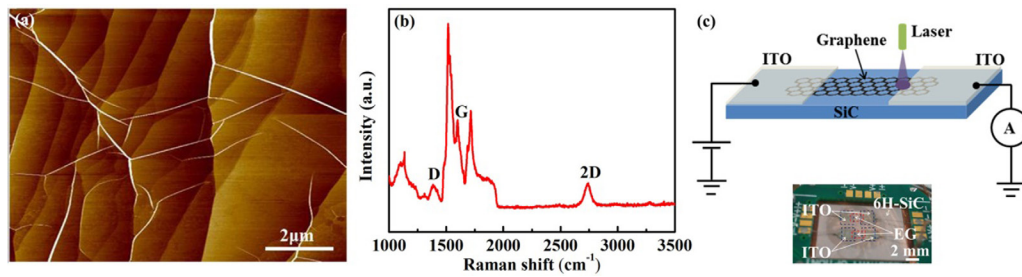[7] Author to whom any correspondence should be addressed.

Figure 1. (a) AFM image of the EG that was grown on the C-face of a semi-insulated 6H–SiC substrate for PSGP. (b) Raman spectrum of the EG. (c) Schematic structure of PSGP together with its optical image.

[4, 6–11], low dark current [4, 7–10], high on-off ratio [4, 5, 7–10], and low noise equivalent power [4, 7]. However, there is a serious limitation here that the speed of response ranges from microseconds to seconds [4–11] mainly due to the fact that the photoexcited carriers must pass through the bulk of the semiconductor. Moreover, the vertical structure is inconvenient to integrate with modern semiconductor planar process technology. On the contrary, the metal–graphene–metal device has a simpler structure with ultrafast response speed [13–17, 20], despite the low responsivity (several mA W^{-1}) observed due to the weak absorption of graphene. To improve the responsivity of metal–graphene–metal devices, various enhancement schemes were adopted, such as hybrid quantum dots [21–23], plasmon effect [24, 25] and optical microcavity or planar photonic crystal cavity [26–31]. However, these complicated processes undoubtedly increase the difficulty in device fabrication and integration with modern semiconductor technology for practical applications. If a supporting substrate for graphene can be used as the medium for enhancing photodetection, the advantages of a planar structure graphene photodetector (PSGP) can be further developed and utilized. Furthermore, the simple planar graphene device is entirely compatible with the modern semiconductor fabrication technology. Recently, Chen *et al* [32] reported a field-enhanced photoactive effect on a graphene photodetector, where position-dependent and millimetre-range photodetection capability was demonstrated in a phototransistor with micrometre-scale graphene on SiC. In a previous study [19], we had also reported that a self-powered and sensitive UV photodetector could be realized using an epitaxial graphene (EG) on a SiC substrate by local irradiation on one of the electrodes. The above studies indicate that both light irradiation and the SiC substrate play very important roles in enhancing the performance of a graphene-based photodetector. Apart from the light source and the substrate, the type of electrode is a major factor that influences the characteristics of a graphene-based photodetector. Usually, metal or conductive indium tin oxide (ITO) semiconductor is adopted as the electrode. In the present study, ITO was selected as the electrode material for the PSGP on SiC, which revealed some new phenomena.

Here, the rectified photocurrent characteristics similar to those in a vertical structure graphene/semiconductor junction photodiode were found in a simple PSGP with ITO symmetrical electrodes on 6H–SiC substrate by local irradiation of UV light. The photocurrent of the device displays a rectified behaviour showing near saturation in forward bias and cutoff in reverse bias. The prototype device fabricated possessed an ultrafast response speed and a moderate responsivity. The governing mechanism behind the observed photocurrent behaviour is attributed to the synergetic effects of the existing small potential barrier at the EG/ITO heterojunction, a local UV illumination on one of the edges between graphene and ITOs, together with a sensitive modulation of applied bias on the transport behaviour of the photogenerated carriers in the SiC near/in the device area. The detailed mechanism has been explained and discussed in the following sections. To the best of our knowledge, the demonstrated photodiode-like behaviour is novel and has not been reported for PSGP.

2. Experimental section

The EG samples were grown on semi-insulated 6H–SiC $(000-1)$ substrates by thermal decomposition of SiC at 1350 °C under forming gas (H$_2$/Ar) ambient. The quality of the as-grown EG samples was evaluated by atomic force microscopy (AFM) (Model: Multimode 8.0, Bruker) and Raman spectroscopy (Model: JY-T64000, Jobin Yvon) before device fabrication, as shown in figures 1(a) and (b), respectively. In the Raman spectrum, it is seen that the Raman peak intensity positioned at 1519 cm^{-1}, which originates from SiC, is far stronger than that of the G peak from EG; and the D peak is weak. All of these indicate that the EG film was less than five layers with a high quality [33, 34]. Using the EG samples, the millimetre-size ITO-graphene-ITO two-terminal prototype devices were fabricated with 1 mm long EG channel and two ITO electrodes (2×2 mm^2, 80 nm thick), as shown schematically in figure 1(c) together with the corresponding optical image. A detailed description of the device fabrication is given in S1 of the supplementary data. The electrical properties of the individual EG and ITO films were characterized by Hall measurement at room temperature using Van der Pauw devices in sizes of 10 mm $\times$ 10 mm. The contact resistance between EG and ITO was measured using a transmission line method and yielded several hundreds of ohms, as given in S2 of the supplementary data. This confirmed that the contact between EG and ITO is near-ohmic. The carrier mobility of EG is about 595 cm^2 V^{-1} s^{-1} with p-type carrier concentration of about 1.4×10^{13} cm^{-2}. The ITO film has a resistivity of about 3.9×10^{-4} $\Omega \cdot$ cm, and the carrier mobility and concentration are about 20 cm^2 V^{-1} s^{-1} and 7.9×10^{20} cm^{-3}, respectively. These values are typical in ITO films deposited by RF magnetron sputtering [35]. For

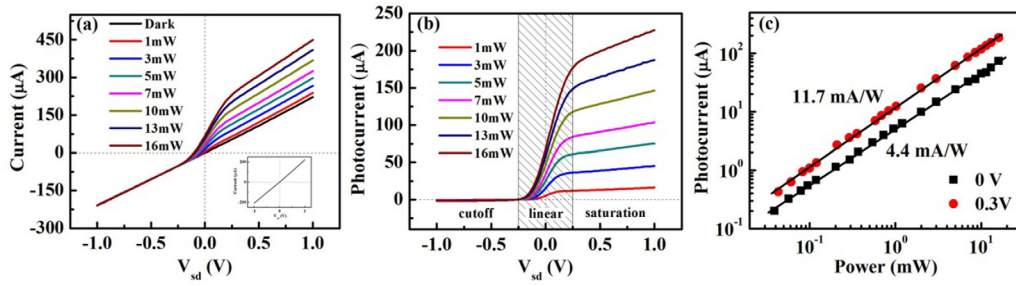J. Phys. D: Appl. Phys. **50** (2017) 405102

J Yang *et al*

Figure 2. Device performance of PSGP. (a) and (b) *I–V* curves and the dependence of net photocurrent on bias voltage, respectively, under UV light (1, 3, 5, 7, 10, 13 and 16 mW) irradiation. The inset in (a) is the dark current curve. (c) Dependence of photocurrent on laser power, at conditions of zero bias (represented by full black squares) and 0.3 V bias (full red circles).

photocurrent measurements, a He–Cd laser of wavelength 325 nm and a Keithley 2400 source meter were employed. The fabricated devices were placed in a vacuum container to avoid influence from atmospheric gases and moisture. The UV light was focused to a spot of diameter about 150 μm on the device. In addition to the steady state optical response, the transient response of the device was measured using a Nd:YAG picosecond pulse laser. The laser parameters were as follows: wavelength 355 nm, pulse duration 25 ps, and repetition rate 1 kHz for a light spot size about 100 μm in diameter. The transient photocurrent profile was recorded in a digital signal oscilloscope (Instrument Model: Tektronix TDS 7254B) having 50 ohm termination and 2.5 GHz bandwidth. The transient response of PSGP was measured at zero bias using different UV pulses of energy ranging from 1 μJ to 8 μJ. In addition, the dependence of photocurrent on light spot position and the variation of photocurrent stability with time were measured and are given in S3 and S4 of the supplementary data, respectively. A comparison of temporal photoresponses of PSGP at zero bias under on-off switching of 325 nm and 632.8 nm light is given in S5.

3. Results and discussion

3.1. Optoelectronic performance of the PSGP

Typical electrical characteristics of the PSGP with and without UV light irradiation are shown in figure 2(a). It is seen that an unusual photocurrent behaviour is observed under opposing biases when the applied bias (V_{sd}) was swept from -1 V to 1 V by local irradiation of UV light, although an almost linear *I–V* curve is observed in dark as amplified in the inset of figure 2(a). Interestingly, the nature of *I–V* characteristic of our device at different laser power is not as similar to that of the traditional metal–graphene–metal photodetector in our early findings [19], but more or less similar to that of a graphene/semiconductor Schottky junction photodiode [4–8, 10]. In order to elucidate the photocurrent mechanism clearly, the variation of net photocurrent I_{ph} (defined as $I_{ph} = I_{UV} - I_{dark}$, where I_{UV} and I_{dark} are measured currents under conditions with and without UV irradiation, respectively) with bias at different UV light intensities was plotted. This is shown in figure 2(b). It is clearly seen from the figure that the net photocurrent variation can be divided into three different regions. In

the negative bias regime (less than -0.25 V), I_{ph} is very small (several microamperes); this is named as the cutoff region. As the bias varies from -0.25 V to 0.25 V (shadowed region in figure 2(b)), photocurrent I_{ph} rises linearly with an increase in applied bias and this is designated as the linear region. When the bias increases beyond a critical value of about 0.25 V, the rate of increase of I_{ph} diminishes and it reaches a saturation level (hundreds of microamperes) with a relatively lower dependence on bias; this is denoted as the saturation region. The quantitative relationship between I_{ph} and V_{sd} in the saturation and linear regions has been estimated and this is included under S6 of supplementary data. It is worth noting that the values of slope and intercept (on photocurrent axis) for each I_{ph} curve in the saturation region are linearly dependent on laser power. This implies that the relationship between photocurrent and bias voltage at a given laser power is predictable and, consequently, an optimum design could be formulated for photodetection applications. The features of the planar device (PSGP) are far superior to those of a vertical structure graphene/semiconductor photodetector; in the latter, the I_{ph}–V relationship under different laser power is usually complex or, even difficult to express in terms of a simple formula due to changes occurring in the Schottky barrier height between the graphene and the semiconductor.

It is seen in figure 2(c) that, at 0.3 V bias, I_{ph} increases linearly with increase in laser power in the measured power range without any sign of saturation, and that its measured slope (responsivity) is 11.7 mA W^{-1}. This translates to an external quantum efficiency of 4.5% for the conversion of photons to conducting electrons; this is relatively small due to extremely small ratio of light spot area to graphene area under irradiated ITO electrode. A broad band of linear response, nearly three orders of magnitude, indicates that the PSGP possesses a wide dynamic range, a prerequisite for any photodetector. At zero bias, the PSGP serves as a self-powered UV photodetector with a reasonable value of responsivity (4.4 mA W^{-1}); it is also enabled by the linear-dependent behaviour of I_{0ph} (as a function of optical power) without attaining saturation levels. This is similar to the behaviour of I_{ph} (see figure 2(c)). In addition, the lowest response power thresholds at zero and 0.3 V biases are about 0.50 μW and 0.35 μW, respectively, which are linear extrapolated from the photocurrent curves as shown in figure 2(c) relative to the noise equivalent current 3.6×10^{-9} A.
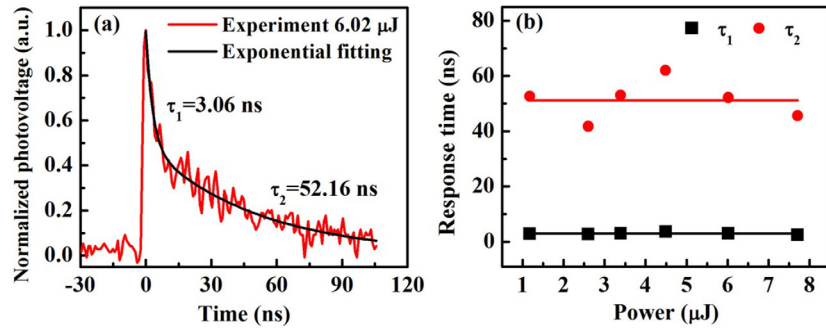
Figure 3. (a) Transient response spectrum of photovoltage from PSGP at zero bias irradiated with a picosecond pulse laser of wavelength 355 nm at repeat frequency of 1 kHz. (b) Response time of PSGP at zero bias recorded for different pulse laser energies; the average values of τ_1 and τ_2 are indicated by black and red lines, respectively.
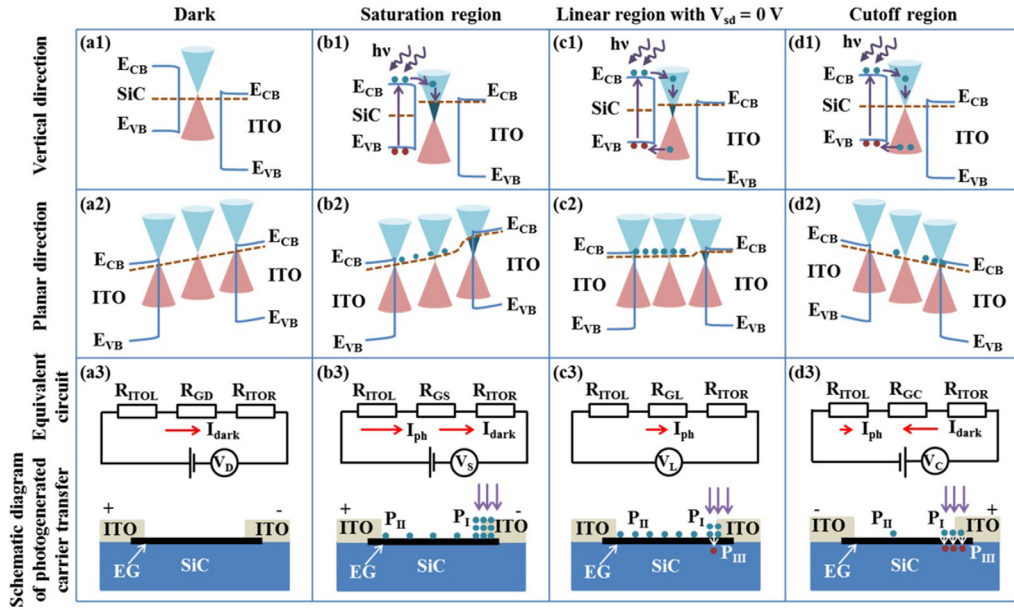

Figure 4. Schematic energy band diagrams of the heterojunction components along vertical (top panels from (a1) to (d1)) and planar (middle panels from (a2) to (d2)) directions and the equivalent circuits as well as schematic photogenerated carrier transfer routes in PSGP in upper and bottom panels of (a3)–(d3), respectively. (ai)–(di) ($i = 1$, 2 and 3) represent the various regions proposed in this study: dark (without UV illumination), saturation, linear and cutoff (with UV illumination) regions.

3.2. Transient response of the PSGP

One typical transient response of the device at zero bias measured with a single pulse of energy 6.02 μJ is shown in figure 3(a). The decay curve of the photovoltage was fitted to the double exponential decay model. It was found that the curve could be fitted well using an ultrafast decay channel with lifetime (τ_1) 3.06 ns and a slightly slower decay channel with lifetime (τ_2) 52.16 ns. All the deduced decay lifetimes under different pulse energies are shown in figure 3(b). It is noted the average value of the fast response lifetime (τ_1) and the slow response lifetime (τ_2) for PSGP are 3 ns and 51 ns, respectively. This indicates the photovoltage decay is less than 40% of its initial value within 3 ns and suggests our PSGP can work at a frequency near gigahertz. It is estimated that the length of graphene channel is about 1 mm, while the average speed of carriers in graphene is assumed as 10^6 m s^{-1}; it can be logically understood that the carrier relaxation time through diffusion in graphene is in the nanosecond range, which is comparable to the fast decay time constant of

3 ns. The slow decay channel in PSGP is believed to be due to carrier relaxation in the interface between graphene and SiC, where photogenerated carriers relax back to SiC through the interface.

3.3. Analysis and discussion

To gain insight into the physical mechanisms that govern the photodiode-like behaviour under locally irradiated UV light, the energy band diagrams of the active components of PSGP were considered for analysis. In top and middle panels of figure 4, the diagrams give schematic energy band configurations of the heterojunction interfaces correspondingly along vertical and planar directions. In the figure, E_{CB} and E_{VB} represent the conduction band and valence band edges, respectively, of SiC or ITO, the dashed dark orange lines represent the Fermi levels of the components, and the aqua green and dark red filled circles represent the photogenerated electrons and holes, respectively. In the bottom panel of figure 4, the

J. Phys. D: Appl. Phys. **50** (2017) 405102

J Yang *et al*

diagrams schematically show the equivalent circuits and the possible photogenerated carrier transfer routes in different regions. Red arrows in equivalent circuits schematically express the direction and the intensity of dark current (I_{dark}) and photocurrent (I_{ph}). R_{ITOm} ($m = L, R$; for left and right electrodes, respectively) represents the resistance of ITO electrode including the contact resistance with graphene, and R_{Gn} ($n = D, S, L$ and C) symbolizes the effective resistance of graphene in dark, under saturation, linear and cutoff regions. It is found that the $R_{GD} \cong R_{GC}$, while $R_{GL} < R_{GS} < R_{GC}$ as supported by figure S7 in the supplementary data.

In the absence of UV light (in dark), there are no photogenerated carriers from SiC transfer to graphene. The schematic energy band configurations are shown in figures 4(a1) and (a2), respectively. The contact potential barrier between ITO and graphene is deduced to be about 60 meV from surface potential measurement as shown in S8 of the supplementary data; this is too small to be reflected, so that a linear *I–V* curve is observed as supported by the inset of figure 2(a).

When the UV light was irradiated, schematic energy band diagrams of the heterojunction components along vertical (top panels from (b1) to (d1)) and planar (middle panels from (b2) to (d2)) directions, and the equivalent circuits as well as the possible photogenerated carriers transfer and relaxation channels (down panels from (b3) to (d3) in the three regions are given in figure 4(bi), (ci) and (di) ($i = 1, 2$ and 3), respectively. At first, we focus attention on the photogenerated carriers in SiC, which is in part transferred to graphene driven by the interface field as discussed in our early work [19]. While the transferred carriers from SiC to graphene underwent at least three major physical processes to reach its steady state, where the carriers being trapped or recombined with existed defects in graphene are neglected to grasp the major aspects to govern the observed phenomena. The three major processes are designated as process I, II and III (symbolized by P_I, P_{II} and P_{III}, respectively) and shown in the bottom panel of figure 4. It is the difference in relative contribution from each process, which is critically dependent on the applied bias, determines the final observed results. In process I, it was considered that carriers remain at the irradiated graphene and electrode to contribute an equivalent potential (V_n) expressed by $V_n = V_{nL} - V_{nR}$ defined as an equivalent potential difference between left and right electrode in dark and the three regions (under UV light), respectively. Here, the subscript *n*, defined for *D, S, L* and *C*, represents four cases in dark, saturation, linear and cutoff regions, respectively. It is found that $V_D = V_C = 0$ and $V_S > V_L > 0$ as supported by figures 2(a) and S7. In process II, carriers migrate along the graphene channel to contribute extra conduction carriers compared with that in the dark condition; this is also equivalent to a total effect of graphene Fermi level raised. In process III, carriers relaxed back into SiC through the interface between graphene and SiC, as schematically shown in figure 4(d1), which is a dominant process in the cutoff region. Therefore, completely different phenomena observed in our PSGP device from the usual planar metal–graphene–metal photodetector critically depend on the applied bias, device structural parameters as contact potential barrier between graphene and ITO, and

device resistance etc. Here, the device structure parameters determine the crossover bias between the cutoff and linear regions, linear and saturation regions, while the applied bias critically changes the relative contributions of each process in our PSGP device.

In the saturation region as described in figure 4(bi), the processes I and II are major contributors, while process III is strongly suppressed. In this case, majority of the transferred carriers remain in the graphene and ITO electrode under the irradiation area, and causes the Fermi level of the graphene to rise significantly. Consequently, an equivalent potential of V_S is generated between the two electrodes, whose magnitude is around hundreds of millivolts, as shown in S7 of supplementary data. In the meantime, few carriers migrate to the graphene channel driven by the applied bias; that causes the Fermi level to rise slightly. This is illustrated by the aqua green filled circles in figure 4(b2). A small upturn in the I_{ph}–*V* curves in the saturation region as seen in figure 2(b). The effect is also equivalent to extra carriers participating conduction compared with that in the dark. This results in a slight reduction of graphene resistance R_{GS} as supported in S7 of the supplementary data. The processes P_I and P_{II} are schematically shown in the bottom panel of figure 4(b3) and an equivalent circuit is also given there.

In the linear region, as shown in figure 4(ci), where the applied bias ranges between -0.25 and 0.25 V, the zero bias level is chosen to represent the entire regime. The other cases can be visualized from the limit values within the corresponding regions. At zero bias, there is no dark current and the net effect of the three processes I, II, and III is reflected in the photocurrent driven by the built-in photovoltage V_L; the magnitude of V_L was deduced as about one hundred millivolts from figure 2(a) and the quantitative estimate of the variation of V_L with laser power is given in S7 of supplementary data. Here, the process II is the most prominent as schematically drawing in figure 4(c2). That is supported by a large slope of the photocurrent increasing with voltage as observing the shadow region in figure 2(b). It is also means the equivalent Fermi level of graphene is raised. So the equivalent resistance of graphene (R_{GL}) is obviously smaller compared with that in dark as supported by figure S7. Compared with the saturation region, the contribution of process II is enhanced because the built-in photovoltage is more effective over the applied bias. This leads to prominent diffusion of photogenerated carriers from the irradiated area into the graphene channel. In addition, process III should be existed and stronger compared with that in saturation region. That is inferred from the fact that a smaller photovoltage is observed in the linear region compared with that in the saturation region as supported by figure S7(a) in supplementary data. The synergetic actions of the three processes render the device a linear dependence on the applied bias and a significant function for self-powered UV photodetectors.

In the cutoff region, the magnitude of the photocurrent is small, ~1 μA, which is almost two orders smaller than that in the saturation region. Here, processes I and II are very weak or negligible, while process III is the dominant one. This means that most of the photoexcited carriers transferred

J. Phys. D: Appl. Phys. **50** (2017) 405102

J Yang *et al*

from SiC to graphene at the irradiated area relaxed back to SiC through the interface, as schematically drawn in figure 4(d1) and in the bottom schematic of figure 4(d3). This process is entirely different from that observed in our early similar device with two metal electrodes [19], where the built-in photovoltage has no relation with the applied bias but was only dependent on the laser power used for irradiation. The only difference between the two devices was the type of electrode used. In the present study, ITO is used in place of the Ti/Au electrode used earlier. It is well known that ITO is a transparent electrode, and also a heavily doped semiconductor [36]. Although it yields an almost (ideal) linear *I–V* curve in the dark, there is more or less of a potential barrier existing between graphene and ITO as supported by analysis in S2 and S8 of the supplementary data. It is the barrier that hinders the photogenerated carriers in graphene to transfer into ITO to form the photocurrent under a reverse bias. Furthermore, under reverse bias, the applied electric field also hinders most of the transferred carriers in graphene migrated into the graphene channel. This implies a weak process II (see figure 4(d2) and the bottom schematic of figure 4(d3)). Therefore, the obstructed carriers naturally form an internal carrier flowing route from SiC to graphene, and finally return to SiC. The internal recycling process is illustrated in figure 4(d1) and in the bottom schematic of figure 4(d3). Therefore, the net effect is that no photocurrent is discernible in this situation.

Based on the experimental results and analysis above, it is supposed that the synergetic actions of the local irradiated UV light, sensitive Fermi level variations in graphene and a moderate potential barrier height between graphene and ITO render the PSGP a prominent and characteristic photodiode-like behaviour. Further correlation of the observed results with device structural parameters in a real PSGP is under progress.

4. Conclusion

In summary, a simple PSGP with typical photodiode-like behaviour has been demonstrated. The prototype photo-detector possesses a working frequency near gigahertz. At 0.3 V bias, it can work as a sensitive UV photodetector with responsivity of 11.7 mA W^{-1}. At zero bias, it functions as a self-powered UV photodetector with responsivity of 4.4 mA W^{-1}. In addition, the wide dynamic linear photoresponse range and predictable relationship between photocurrent and bias voltage at different laser powers strongly suggest that the PSGP design could be optimized to realize a high performance photodetector. The advanced functional features and superior performance of the PSGP are attributed to the unique properties of graphene, especially its sensitive Fermi level variation and high carrier mobility, custom-designed planar structure using ITO electrodes and localized irradiation by UV light that facilitates absorption by the SiC substrate. The novel properties and simple fabrication steps of our PSGP are likely to pave new ways to realize ultrafast graphene-based planar photodiodes for use in opto-electrical integrated circuits.

Appendix. Supplementary data

Supplementary data related to this article can be found at (stacks.iop.org/JPhysD/50/405102/mmedia)

References

[1] Bolotin K I *et al* 2008 Ultrahigh electron mobility in suspended graphene *Solid State Commun.* **146** 351–5

[2] Peres N M R 2010 Colloquium *Rev. Mod. Phys.* **82** 2673–700

[3] Bonaccorso F, Sun Z, Hasan T and Ferrari A C 2010 Graphene photonics and optoelectronics *Nat. Photon.* **4** 611–22

[4] An X, Liu F, Jung Y J and Kar S 2013 Tunable graphene–silicon heterojunctions for ultrasensitive photodetection *Nano Lett.* **13** 909–16

[5] Lin F *et al* 2014 Graphene/GaN diodes for ultraviolet and visible photodetectors *Appl. Phys. Lett.* **105** 073103

[6] Zhu M *et al* 2014 Vertical junction photodetectors based on reduced graphene oxide/silicon Schottky diodes *Nanoscale* **6** 4909–14

[7] Li X *et al* 2016 High detectivity graphene-silicon heterojunction photodetector *Small* **12** 595–601

[8] Xu K *et al* 2015 Graphene GaN-based Schottky ultraviolet detectors *IEEE Ttans. Electron Devices* **62** 2802–8

[9] Li X *et al* 2016 Graphene/h-BN/GaAs sandwich diode as solar cell and photodetector *Opt. Express* **24** 134–45

[10] Kumar M, Jeong H, Polat K, Okyay A K and Lee D 2016 Fabrication and characterization of graphene/AlGaN/GaN ultraviolet Schottky photodetector *J. Phys. D: Appl. Phys.* **49** 275105

[11] Liu F and Kar S 2014 Quantum carrier reinvestment-induced ultrahigh and broadband photocurrent responses in graphene–silicon junctions *ACS Nano* **8** 10270–9

[12] Chao L, Peng Z and David Wei Z 2017 Devices and applications of van der Waals heterostructures *J. Semicond.* **38** 031005

[13] Xia F, Mueller T, Lin Y-M, Valdes-Garcia A and Avouris P 2009 Ultrafast graphene photodetector *Nat. Nanotechnol.* **4** 839–43

[14] Mueller T, Xia F and Avouris P 2010 Graphene photodetectors for high-speed optical communications *Nat. Photon.* **4** 297–301

[15] Urich A, Unterrainer K and Mueller T 2011 Intrinsic response time of graphene photodetectors *Nano Lett.* **11** 2804–8

[16] Singh R S, Nalla V, Chen W, Ji W and Wee A T S 2012 Photoresponse in epitaxial graphene with asymmetric metal contacts *Appl. Phys. Lett.* **100** 093116

[17] Sun D *et al* 2012 Ultrafast hot-carrier-dominated photocurrent in graphene *Nat. Nanotechnol.* **7** 114–8

[18] Sun R *et al* 2013 Tunable photoresponse of epitaxial graphene on SiC *Appl. Phys. Lett.* **103** 013106

J. Phys. D: Appl. Phys. **50** (2017) 405102

J Yang *et al*

[19] Jiao H *et al* 2016 A self-powered sensitive ultraviolet photodetector based on epitaxial graphene on silicon carbide *Chin. Phys.* B **25** 067205

[20] Cheng C *et al* 2017 Frequency conversion with nonlinear graphene photodetectors *Nanoscale* **9** 4082–9

[21] Konstantatos G *et al* 2012 Hybrid graphene-quantum dot phototransistors with ultrahigh gain *Nat. Nanotechnol.* **7** 363–8

[22] Son D I, Yang H Y, Kim T W and Park W I 2013 Photoresponse mechanisms of ultraviolet photodetectors based on colloidal ZnO quantum dot-graphene nanocomposites *Appl. Phys. Lett.* **102** 021105

[23] Haider G *et al* 2016 Electrical-polarization-induced ultrahigh responsivity photodetectors based on graphene and graphene quantum dots *Adv. Funct. Mater.* **26** 620–8

[24] Echtermeyer T J *et al* 2011 Strong plasmonic enhancement of photovoltage in graphene *Nat. Commun.* **2** 458

[25] Freitag M, Low T, Zhu W, Yan H, Xia F and Avouris P 2013 Photocurrent in graphene harnessed by tunable intrinsic plasmons *Nat. Commun.* **4** 1951

[26] Engel M *et al* 2012 Light–matter interaction in a microcavity-controlled graphene transistor *Nat. Commun.* **3** 906

[27] Furchi M *et al* 2012 Microcavity-integrated graphene photodetector *Nano Lett.* **12** 2773–7

[28] Pospischil A *et al* 2013 CMOS-compatible graphene photodetector covering all optical communication bands *Nat. Photon.* **7** 892–6

[29] Wang X, Cheng Z, Xu K, Tsang H K and Xu J-B 2013 High-responsivity graphene/silicon-heterostructure waveguide photodetectors *Nat. Photon.* **7** 888–91

[30] Shiue R-J *et al* 2015 High-responsivity graphene–boron nitride photodetector and autocorrelator in a silicon photonic integrated circuit *Nano Lett.* **15** 7288–93

[31] Shiue R-J *et al* 2013 Enhanced photodetection in graphene-integrated photonic crystal cavity *Appl. Phys. Lett.* **103** 241109

[32] Sarker B K, Cazalas E, Chung T-F, Childres I, Jovanovic I and Chen Y P 2017 Position-dependent and millimetre-range photodetection in phototransistors with micrometre-scale graphene on SiC *Nat. Nanotechnol.* **12** 668–74

[33] Ni Z H *et al* 2008 Raman spectroscopy of epitaxial graphene on a SiC substrate *Phys. Rev.* B **77** 115416

[34] Shivaraman S, Chandrashekhar M V S, Boeckl J J and Spencer M G 2009 Thickness estimation of epitaxial graphene on SiC using attenuation of substrate Raman intensity *J. Electron. Mater.* **38** 725–30

[35] Hu Y, Diao X, Wang C, Hao W and Wang T 2004 Effects of heat treatment on properties of ITO films prepared by rf magnetron sputtering *Vacuum* **75** 183–8

[36] Minami T 2005 Transparent conducting oxide semiconductors for transparent electrodes *Semicond. Sci. Technol.* **20** S35–44